Classical, quantum, and thermodynamics of a lattice model exhibiting structural negative thermal expansion

Connor A. Occhialini,[1] Sahan U. Handunkanda,[1,2] Erin B. Curry,[1,2] and Jason N. Hancock[1,2]

[1]*Department of Physics, University of Connecticut, Storrs, Connecticut 06269, USA*

[2]*Institute for Materials Science, University of Connecticut, Storrs, Connecticut 06269, USA*

We consider in detail a simple model supporting a single floppy mode that is often used to heuristically describe instances of negative thermal expansion. A key result is that the translational kinetic energy of the dilating bond network scales extensively with system size and results in dynamical properties which differ qualitatively from considerations built upon harmonic models. We develop an analogy between the dynamics of this model and a modified mechanical pendulum to elucidate the connection between the new results and the familiar harmonic limit. We then propose an appropriate Schrödinger equation for this system and study numerically the quantum mechanical solutions. Marked differences from conventional phonon dynamics and thermodynamics are seen in both classical and quantum limits, in particular a strong twofold enhancement of the (negative) coefficient of thermal expansion. We contextualize the results against real material parameters and discuss related empirical observations.

Negative thermal expansion (NTE) has been identified from the early 20th century as a maverick phenomenon [1], and two routes to realizing this effect have been identified: (i) broadened phase transitions and (ii) intrinsic structural origins. Investigations into the first class of NTE phenomena have revealed contentious issues regarding the interplay of magnetism, disorder, charge disproportionation, and their volume coupling and continue to intrigue physicists [2–8]. The second class of behavior, which we term structural NTE (SNTE), is observed in both metallic and insulating materials without competing order [9–14]. SNTE arises instead from the low-energy fluctuations of the bond network which draw in the lattice when thermally activated and represents a particularly interesting limit of lattice dynamics.

A central question in the study of SNTE is whether basic structural mechanics principles and intuition can be applied to guide discovery of new materials that display this anomalous effect. For example, metallic ReO_3 and insulating ScF_3 with open perovskite structure display SNTE over a wide range of temperatures [15,16], but why do other open perovskites most commonly exhibit positive thermal expansion (PTE)? Why is SNTE so rare, inevitably yielding to PTE in response to disorder [16–18] and application of pressure? In pursuit of conceptual control of the phenomenon, innovative approaches have been offered which link thermally activated transverse vibration of structural units to a tendency to draw in lattice dimensions. "Rigid unit" approaches view polyhedral molecular units (i.e., metal-anion tetrahedra and octahedra) rather than ions as the fundamental building blocks of a material and attempt to link the states built from rotational zero modes of the free molecules to the low-energy modes of the crystal. In this view, intramolecular degrees of freedom are effectively integrated out, and the nature of their coordinated motion as a function of lattice topology and connectivity [19–23] is the central feature of SNTE. New discoveries of robust SNTE have reinvigorated the field and raised the question of whether strict molecular rigidity is an appropriate starting point [24–26] or if, instead, it is more appropriate to consider only the rigidity of the stiffest bonds in a view of the

materials as a framework of struts. In an effort to advance the relative importance of molecular or bond stiffness in SNTE systems, the present paper regards analytical and numerical descriptions of a simple model supporting a single collective mode capable of producing SNTE.

A two-dimensional constrained lattice model (2D CLM) is shown in Fig. 1. The finite crystal consists of corner-linked diamonds with coordinate origin at the center of mass (c.m.). The diamonds could represent metal-anion octahedra in a perovskite lattice structure such as the strong SNTE systems ScF_3 or ReO_3, but has been used to describe more complex lattices [27–31]. The $N_\diamond = N_x N_y$ diamonds are attached by hinged joints, so that their motional degrees of freedom are constrained. The 2D CLM is an interesting case in that it is isostatic [32–35], or marginally constrained [36,37], in the sense that even in the thermodynamic limit, there is exactly one internal degree of freedom: a staggered rotation of each diamond by an angle θ. When $\theta = 0$, the lattice has the maximum area $A_0 = N_\diamond a_0^2$, but changing θ from zero in either direction contracts the lattice to an area $A_0 \cos^2 \theta$, and thermal activation of this collective mode is often attributed as the origin of NTE [27–31,38].

In addition to computational approaches built around phonons, efforts to develop this model into a field theory which respects the high-energy constraints of bond stretch and bond-bend degrees of freedom include mimicking polyhedral pliancy through a split-atom approach [39], by lowering the degree of constraint [40,41], or permitting some diamonds to be replaced with springs [42], and unusual properties like NTE are found in each case. Below, we fully enforce the constraints and show that exact analytical results link phonon dynamics continuously to the floppy mode (FM) of the 2D CLM. We will see that this strictly rigid limit is inconsistent with the thermodynamic limit and focus our attention to finite lattices. A comparison of emergent properties derived from the 2D CLM Hamiltonian and their crossover from textbook harmonic dynamics is the subject of this paper. We reassess the possible role of molecular rigidity in Sec. IV.
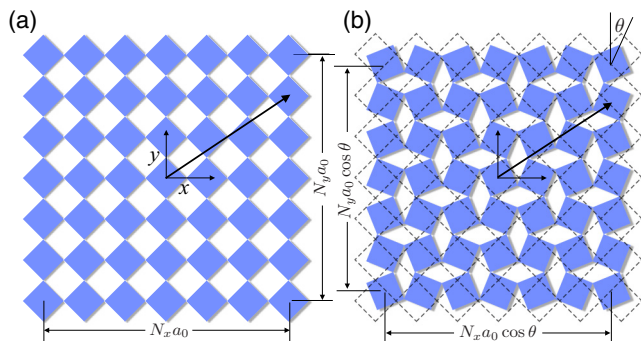
FIG. 1. The two-dimensional constrained lattice model (2D CLM) with staggered angle (a) $\theta = 0$ and (b) $\theta \neq 0$. In the rigid limit, the lattice dimensions contract uniformly by a factor $\cos \theta$.

I. CLASSICAL MECHANICS OF THE 2D CLM

Consider first the kinetic energy of the 2D CLM. When $\theta = 0$, a diamond center can be located at position $\vec{r}(\theta = 0) = (n_x, n_y)a_0$. When $\theta \neq 0$, the distance between neighboring diamond centers is reduced by a multiplicative factor $\cos \theta$ and each position vector is scaled similarly, $\vec{r}(\theta) = (n_x, n_y)a_0 \cos \theta$, with velocity $\dot{\vec{r}}(\theta) = -(n_x, n_y)a_0 \dot{\theta} \sin \theta$. The velocity vectors and position vectors of each diamond always point directly toward or away from the c.m. Summing the translational energy $m_\diamond \dot{r}^2/2$ over all diamonds in the crystal, the total translational kinetic energy is

$$K_\diamond^{\text{trans}} = \frac{1}{2} I_c \dot{\theta}^2 \sin^2 \theta,$$

where $I_c = \sum_{n_x n_y} m_\diamond [(n_x a_0)^2 + (n_y a_0)^2]$ is the moment of inertia of a similar crystal where diamonds are replaced by points, each of mass $m_\diamond$. The appearance of the moment of inertia in the kinetic energy reflects a deep connection between the *staggered* rotation of the 2D CLM and the *uniform* rotation of a rigid body, where dynamical motion is also characterized by a single angle, with velocity increasing linearly with distance from the c.m., but wherein material displacements are purely tangential.

Including the rotational kinetic energy of each diamond and summing, the total kinetic energy of the 2D CLM is

$$K = \frac{1}{2} N_\diamond I_\diamond \dot{\theta}^2 + \frac{1}{2} I_c \dot{\theta}^2 \sin^2 \theta = \frac{1}{2} N_\diamond I_\diamond \dot{\theta}^2 (1 + k^2 \sin^2 \theta),$$
$$(1)$$

where $k = \sqrt{\frac{I_c}{N_\diamond I_\diamond}} = \sqrt{\gamma N_\diamond}$ and $\gamma = I_c/N_\diamond^2 I_\diamond$ depends on the aspect ratio of the crystal and mass distribution for the diamonds (~ 1.79 for a square crystallite of ScF$_3$) [43]. Significantly, the kinetic energy of the FM has a rotational part (the first term) which scales with system size in an *intensive* way ($\propto N_\diamond$), while the translational kinetic energy scales *extensively* ($I_c \propto N_\diamond^2$). In the present work, we study the dynamics of this floppy mode in finite systems.

We introduce a bond-bend potential $V(\theta)$ at each molecular junction to stabilize the equilibrium structure and study dynamical fluctuations about the ground state, where $\theta = 0$. The lowest Fourier component of this potential can be written $\kappa(1 - \cos \theta) \simeq \kappa \theta^2/2$ in the small-angle limit. The energy of the 2D CLM is, therefore,

$$E = \frac{1}{2} N_\diamond I_\diamond (1 + k^2 \sin^2 \theta) \dot{\theta}^2 + N_b \kappa (1 - \cos \theta), \quad (2)$$

where $N_b \simeq 2 N_\diamond$ is the total number of intermolecular linkages. In the small θ limit, this reduces to

$$E = \frac{1}{2} N_\diamond I_\diamond [1 + (k\theta)^2] \dot{\theta}^2 + \frac{1}{2} N_b \kappa \theta^2. \quad (3)$$

Figure 2(a) shows solutions to the equations of motion which can be determined from the inverse of the function,

$$t(\theta) = \frac{1}{\omega_p} \int_0^\theta \sqrt{\frac{1 + k^2 \theta'^2}{\theta_0^2 - \theta'^2}} d\theta'$$
$$= \frac{1}{\omega_p} E\left[\arcsin \left(\frac{\theta}{\theta_0} \right), -k^2 \theta_0^2 \right], \quad (4)$$

valid for $-\theta_0 < \theta < \theta_0$, where $E(\phi, m)$ is the incomplete elliptic integral of the second kind and $\omega_p = \sqrt{N_b \kappa/N_\diamond I_\diamond}$. The $k = 0$ limit returns sinusoidal motion with amplitude θ_0 and frequency ω_p, as expected. Of particular interest, however, is the limit of large k, which corresponds to the thermodynamic limit of the 2D CLM. Equation (4) then permits an exact solution:

$$\frac{(t - t_0)^2}{(k\theta_0/\omega_p)^2} + \frac{\theta^2}{\theta_0^2} = 1.$$

The time-dependent staggered angle can be described by waves constructed from semicircular arcs in the θ-t plane, in contrast to the familiar sinusoidal behavior of the harmonic limit.

Several aspects of the thermodynamic FM are distinct from the harmonic case: (i) the period $\tau = \frac{4k\theta_0}{\omega_p} = 4\theta_0 \sqrt{\frac{I_c}{N_b \kappa}}$ is proportional to both the amplitude of oscillation and the system size, (ii) the system spends vanishingly small time in
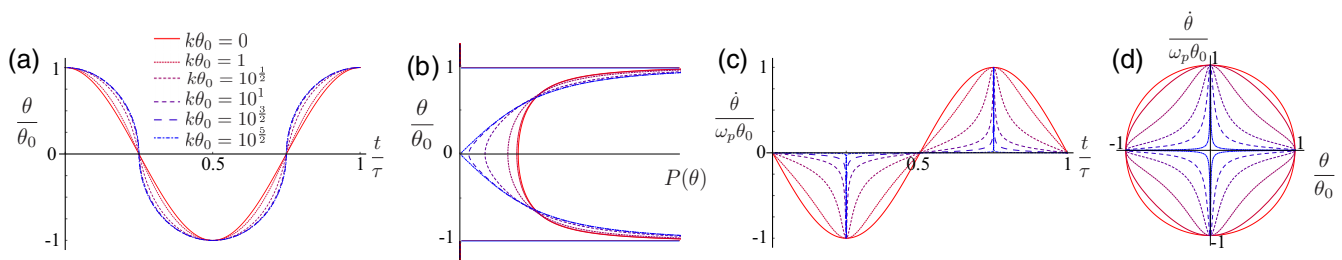

FIG. 2. Panels (a)–(d) show classical solutions for $\theta(t)$ which follow from Eq. (3). These are plotted for different values of $k\theta_0$, which uniquely quantifies the anharmonic behavior. The time axes in (a) and (c) are scaled by the FM period.

the average position, and (iii) $P(\theta)$ shows enhanced variance [Fig. 2(b)], spending far more time near the extrema. These three counterintuitive features are described in a different context in Sec. 1 of the Appendix, which identifies the dual problem of the Archimedean spherical pendulum (ASP): a particle confined to an Archimedean spherical helix moving under the influence of local gravity.

II. QUANTUM MECHANICS OF THE 2D CLM

In this section, we quantize the 2D CLM in the small-angle limit. The classical Lagrangian of the 2D CLM/ASP is

$$\mathcal{L} = \tfrac{1}{2} N_\diamond I_\diamond (1 + k^2 \sin^2 \theta) \dot{\theta}^2 - N_b \kappa (1 - \cos \theta).$$

The variable θ has a conjugate momentum,

$$L_\theta = \frac{\partial \mathcal{L}}{\partial \dot{\theta}} = N_\diamond I_\diamond (1 + k^2 \sin^2 \theta) \dot{\theta}.$$

Together, θ and L_θ span phase space, with the classical Hamiltonian

$$H = L_\theta \dot{\theta} - \mathcal{L}$$
$$= \frac{L_\theta^2}{2 N_\diamond I_\diamond (1 + k^2 \sin^2 \theta)} + N_b \kappa (1 - \cos \theta).$$

Expanding for small $\theta < 1$, then substituting $\phi = k\theta$ and $L_\phi = L_\theta / k$, we get

$$H = \frac{k^2 L_\phi^2}{2 N_\diamond I_\diamond (1 + \phi^2)} + \frac{1}{2} \frac{N_b \kappa}{k^2} \phi^2.$$

ϕ corresponds to the azimuthal angle of the ASP, is not necessarily small, and is the natural variable for quantization.

In anticipation of quantizing $L \to i\hbar\partial$, we consider the operator ordering possibilities relevant to the kinetic energy in the last expression. The kinetic energy contains the two usual factors of the conjugate momentum and an additional Lorentzian factor $f = \frac{1}{1+\phi^2}$. These three operators can be arranged in the following inequivalent combinations: $L_\phi^2 f$, $L_\phi f L_\phi$, and $f L_\phi^2$. The requirement that the Hamiltonian be self-adjoint restricts our attention to $L_\phi f L_\phi$ and the symmetric combination $(L_\phi^2 f + f L_\phi^2)/2$. To distinguish between these possibilities, we turn to the correspondence principle for guidance and compare the numerical solutions in each case to the classical time-averaged probability distribution $P_t(\phi)$ [44],

$$P_t(\phi) = \frac{1}{2E(-\phi_0^2)} \sqrt{\frac{1 + \phi^2}{\phi_0^2 - \phi^2}},$$

where $E(x)$ is the complete elliptic integral of the second kind and the classical turning points are $\phi_0 = \pm k\sqrt{2E/N_b\kappa}$. In a side-by-side comparison, we find that the operator choice $(L_\phi^2 f + f L_\phi^2)/2$ produces wave functions that resemble the classical time-averaged probability distributions of Fig. 2(b) and explicit comparison is shown for the 25th excited state in Fig. 3(a). The time-independent Schrödinger equation is therefore

$$\left[-\frac{\hbar^2 k^2}{4 N_\diamond I_\diamond} \left(\frac{1}{1+\phi^2} \partial_\phi^2 + \partial_\phi^2 \frac{1}{1+\phi^2} \right) + \frac{N_b \kappa}{2k^2} \phi^2 \right] \psi = E\psi.$$

Defining scaled energy $\varepsilon = E/\hbar\omega_p$, the dimension-free Schrödinger equation for the 2D CLM is

$$-\frac{\nu}{4} \left(\frac{1}{1+\phi^2} \partial_\phi^2 + \partial_\phi^2 \frac{1}{1+\phi^2} \right) \psi + \frac{1}{2\nu} \phi^2 \psi = \varepsilon \psi, \quad (5)$$

where $\nu = k^2 \hbar / N_\diamond I_\diamond \omega_p$. For small $\phi \ll 1$, Eq. (5) reduces to

$$-\frac{\nu}{2} \partial_\phi^2 \psi + \frac{1}{2\nu} \phi^2 \psi = \varepsilon \psi,$$

which describes the harmonic limit with ground-state uncertainty in the angle $\Delta\phi = \sqrt{\nu/2} = 0.707\sqrt{\nu}$. We therefore expect the harmonic limit [45] to be realized near the condition of ν small, with new anharmonic features for highly excited states and/or ν large. The crossover in behavior is controlled by the dimensionless parameter ν, proportional to $\hbar$:

$$\nu = \frac{k^2}{N_\diamond} \frac{\hbar}{I_\diamond \omega_p} = \frac{I_c}{N_\diamond^2 I_\diamond} \frac{\hbar}{I_\diamond \omega_p} = \gamma \frac{\hbar}{I_\diamond \omega_p}.$$

The factor γ, introduced above, is a number which is of order unity (see Table II) and independent of system size for large systems. The remaining factor $\hbar/I_\diamond\omega_p$ compares the quantum of angular momentum $\hbar$ to the angular momentum of a single diamond rotating at angular frequency ω_p. With a $\hbar\omega_p = 1$ meV oscillation corresponding to the zone edge optical phonon of ScF_3 and many perovskite systems, and using the lattice parameter $a \simeq 4$ Å, we get $\hbar/I_\diamond\omega_p = 0.0273$ and an overall $\nu_{ScF_3} = 0.0491$. Considering ν_{ScF_3}, $\Delta\phi = \sqrt{\nu_{ScF_3}/2} \simeq 0.157$rad $= 8.975°$. $\Delta\phi$ is already appreciable in the ground state, implying that the wave functions are significantly altered from the Hermite polynomial type expected in the pure harmonic limit. Section 3 of the Appendix evaluates γ, ν, and $\Delta\phi$ for some interesting materials.

The effects of nonzero ν on the ground-state wave function are shown in Fig. 3(c), where a general broadening of the probability distribution precedes formation of a two-hump structure for $\nu > 1$, indicating an approach to an instability at zero temperature. One may speculate that this is a signature that dilational dynamics resultant from local rigidity may influence structural phase stability. We stress that $\theta = \phi/k = \phi/\sqrt{\gamma N_\diamond}$ is the physical angle so the quantum fluctuations ϕ are suppressed by the system size: $\Delta\theta \to 0$ in the strict thermodynamic limit.

III. THERMODYNAMICS OF THE 2D CLM

The quantized energy spectrum shows sublinear dependence on quantum number [Fig. 3(d)], but the harmonic limit is recovered for $\nu \to 0$, as expected. The variance $\langle n|\phi^2|n\rangle$ is shown versus energy in Fig. 3(e) versus the scaled energy $\varepsilon = E/\hbar\omega_p$ (solid lines) along with the same result for an Einstein harmonic oscillator (dashes) with the same ground-state uncertainty $\Delta\phi$. We see that NTE is enhanced in the 2D CLM for two reasons: (i) the enhancement of angular fluctuations is larger within each energy window but also (ii) the low-temperature density of states is larger as a result of the strain interactions.

The combined effect of these influences is manifest in the thermally averaged unit-cell dimension, which is directly related to the thermally averaged moments of θ: $a(T) =$

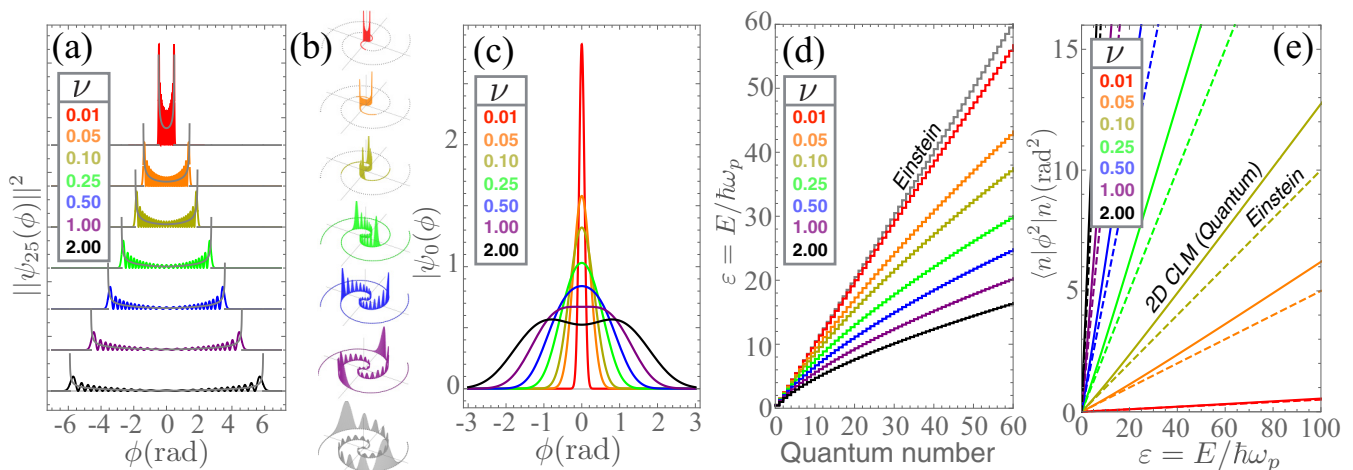FIG. 3. $n = 25$ excited-state wave functions of the quantum 2D CLM in (a) and unfolded; (b) an Archimedean spiral representation for a span of ν values. (c) Ground-state wave functions $\psi_0(\phi)$. (d) Energy spectrum of the quantum 2D CLM, showing convergence to the harmonic limit as $\nu \to 0$. (e) Variance in ϕ versus scaled energy for the 2D CLM (solid) and for the harmonic approximation (dashed) at the same ν, showing the enhancement of angular fluctuations arising from the translational kinetic energy.

$\langle a_0 \cos\theta \rangle \simeq a_0(1 - \langle\theta^2\rangle_T/2) = a_0(1 - \langle\phi^2\rangle_T/2k^2)$, where the expectation value $\langle\,\rangle_T$ is over the statistical distribution. The classical limit permits the analytical result

$$\langle\phi^2\rangle_{T,\text{cl}} = \frac{1}{Z_{\text{cl}}} \int \phi^2 e^{-\beta H} d\phi \, dL_\phi$$

$$= \frac{k_B T k^2}{\frac{1}{2} N_\diamond I_\diamond \omega_p^2} \left\{ \frac{1}{1 + \frac{K_0(\delta)}{K_1(\delta)}} \right\}.$$

with $\beta = 1/k_B T$ and $\delta = N_b \kappa / 4k^2 k_B T = \hbar\omega_p/4\nu k_B T$. The temperature-dependent lattice parameter according to the classical 2D CLM is

$$a_{\text{cl}}(T) = a_0\left(1 - \frac{k_B T}{N_\diamond I_\diamond \omega_p^2} \left\{ \frac{1}{1 + \frac{K_0(\delta)}{K_1(\delta)}} \right\}\right). \quad (6)$$

Welche *et al.* [38] have presented an expression for the 2D CLM excluding the translational kinetic energy and find a T-linear lattice parameter and T-independent negative coefficient of thermal expansion (CTE). The factor in brackets in (6) is new and approaches $\frac{1}{2}$ in the low-T limit and 1 in the high-T limit, suggesting that the translational kinetic energy enhances SNTE significantly. This relative change in lattice parameter is shown as $\Delta a/a_0 = [a(T) - a_0]/a_0$ in Fig. 4(b) for this classical result along with corresponding calculation for the quantum model and various values of ν, showing a general enhancement of slope with increasing ν.

The CTE $\alpha_L = da/dT$ can be calculated straightforwardly from this expression, and we find that the α_L is a universal function of $k_B T\nu/\hbar\omega_p = 1/4\delta$, shown as a thick line in Fig. 4(c):

$$\alpha_L(T) = -\frac{a_0 k_B}{N_\diamond I_\diamond \omega_p^2} \left\{ \frac{1}{1 + \frac{K_0(\delta)}{K_1(\delta)}} - \delta \frac{d}{d\delta} \frac{1}{1 + \frac{K_0(\delta)}{K_1(\delta)}} \right\}. \quad (7)$$

In the absence of translational kinetic energy, the term in brackets is constant and equal to $1/2$ [38], shown as a

dashed line. The new feature resultant from considering the translational kinetic energy is a doubling of the SNTE effect above a crossover temperature $k_B T \simeq \hbar\omega_p/2\nu$. Quantum effects are also apparent in Fig. 4(c) and tend to suppress the CTE at low temperature.

Expressions for the classical thermal energy are given in Sec. 2 of the Appendix and describe the unequal partitioning among the rotational, translational, and potential energy contributions to the thermal energy of the 2D CLM. We present these results as a universal plot in Fig. 5(a) with different contributions shown separately. When k or $\nu \to 0$, the Hamiltonian is equivalent to a harmonic oscillator, the preconditions of the equipartition theorem are valid, and the heat capacity is $C = k_B$, as expected for the two degrees of freedom (rotational kinetic and potential). When $\nu \neq 0$, the additional inclusion of the translational kinetic energy and quartic terms render the equipartition theorem invalid, and even the classical heat capacity depends on temperature. Interestingly, the sum of potential and rotational terms equals k_B independently of ν, but the thermal energy is equally partitioned among these two terms only when $\nu \to 0$. In the large ν limit, the total energy is $3k_B T/2$ distributed as $k_B T$ potential, $k_B T/2$ translational, and negligible rotational energy.

Figure 5(b) shows the heat capacity of the 2D CLM using quantum numerics as a plot of C/T^3 versus $\ln T$, which represents an approximate profile of the vibrational density of states in a phonon interpretation [46–50]. The effect of ν is to increase the low-T heat capacity and distort this function significantly from the Einstein form. Figures 5(c) and 5(d) compare the classical and quantum heat capacity for moderate (0.05) and large (2.0) values of ν. For small ν, the quantum solution appears Einstein-like, with a rapid approach to the classical (Dulong-Petit) limit around $k_B T = \hbar\omega_p$, as expected. For larger ν, distortions from the Einstein form become apparent. In both cases, the quantum and classical limits converge well before the high-temperature limit of $3k_B T/2$ is reached, in contrast to the classical Dulong-Petit/Einstein
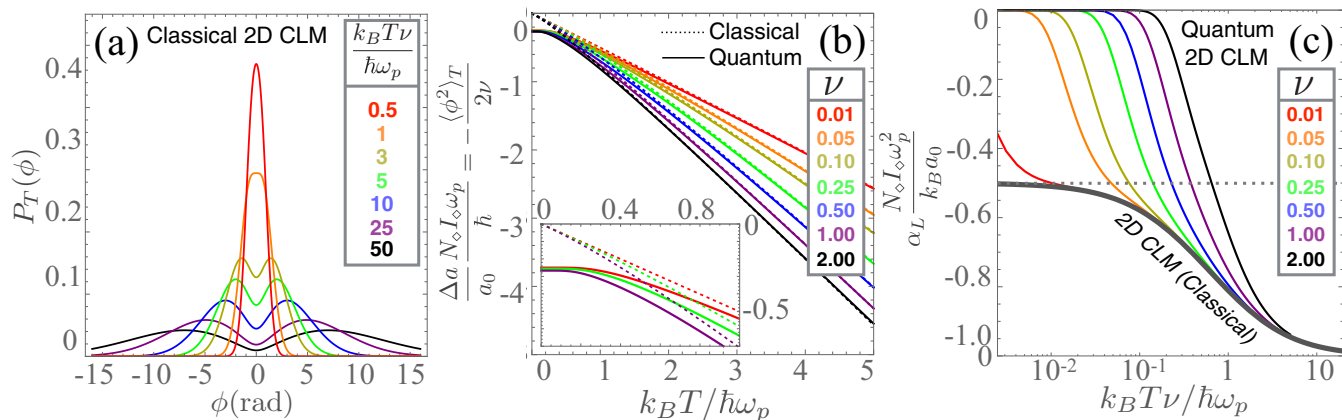
FIG. 4. (a) Thermally averaged probability distribution $P_T(\phi)$ for different values of $k_B T \nu/\hbar\omega_p$, showing the appearance of a node at $\phi = 0$. (b) Relative change in lattice parameter measured in units of $\hbar/N_\diamond I_\diamond \omega_p$ as a function of $k_B T$ in units of $\hbar\omega_p$ according to classical (dashed) and quantum (solid) treatment of the 2D CLM. The inset shows a magnification of the low-temperature behavior for clarity. (c) Linear coefficient of thermal expansion α_L in units of $k_B a_0/N_\diamond I_\diamond \omega_p^2$ as a function of $k_B T \nu/\hbar\omega_p$. The thick gray line shows the universal classical result, starting at a low-T value of $-\frac{1}{2}$ and crossing over to -1 at high temperature, where the translational kinetic energy enhances the SNTE effect. Thin solid lines show the quantum result for different values of ν.

results, which converge to each other and the high-temperature limit simultaneously.

IV. DISCUSSION

The developments presented here are enabled by assuming that a strictly rigid limit is taken in a two-dimensional system, bringing the number of degrees of freedom from a thermodynamic number to a single mode. This residual soft degree of freedom results from integrating out the intramolecular degrees of freedom in an approximation of the strain interactions as having infinite range. While this conceptual convenience has been traditionally invoked to heuristically describe SNTE, whether the strict limit has a place in describing real materials is a rather contentious issue that has been revisited lately.

In the original SNTE material ZrW_2O_8, the role of rigidity has been discussed at length in semiclassical terms [19,22,23,25,51], with a common premise of molecular rigidity but disagreement on the sense of motion required to generate SNTE. ZrW_2O_8 is a complex-structured material with 44 atoms/unit cell and consists of a network of ZrO_6 octahedra and WO_4 tetrahedra with large, open voids, inspiring a rich discussion and proposals that the system is mechanically underconstrained and frustrated [41,48]. More recently, the premise of molecular rigidity has been questioned, and a view of metal-anion bond rigidity [25] has been proposed based on MD simulations.

Recently, strong NTE was discovered in ScF_3, an open perovskite only four atoms/unit cell that remains cubic at all temperatures $T < 1800$ K. This model system has the capacity to shed light on the issue of molecular versus bond rigidity
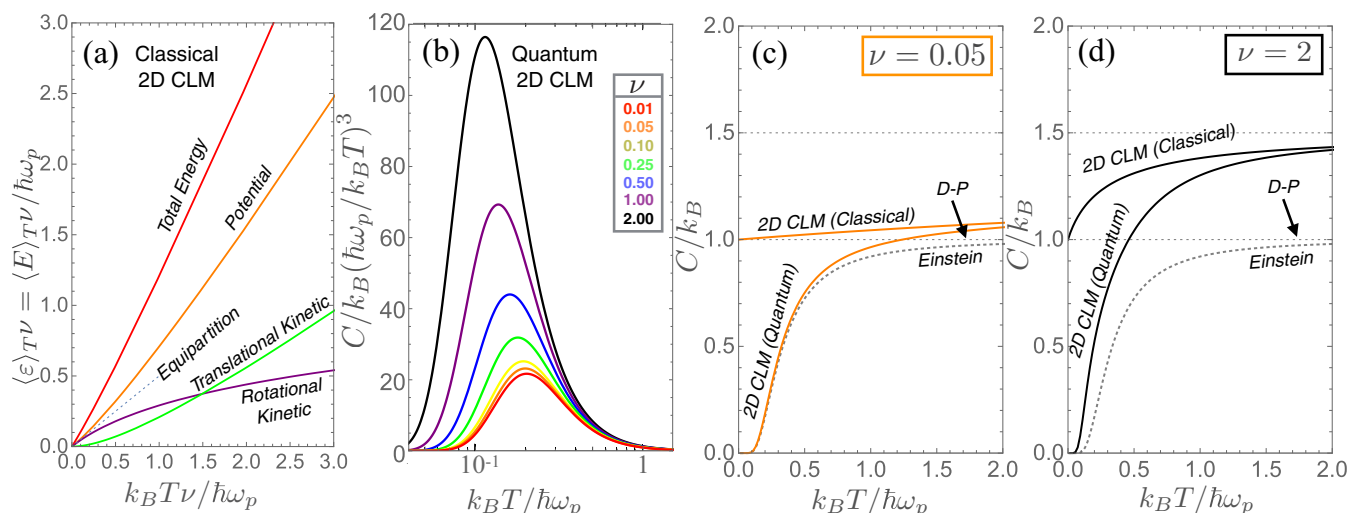

FIG. 5. (a) Classical thermal energy of the model with translational kinetic, rotational kinetic, and potential energy contributions shown explicitly. The dashed line shows the equipartition/Dulong-Petit limit. (b) ν dependence of C/T^3 versus T on a log scale which presents and image of the phonon density of states in a phonon interpretation [46]. Panels (c) and (d) show the heat capacity for the usual Einstein and Dulong-Petit limits along with the classical analytic results and quantum computational results for (c) $\nu = 0.05$ and (d) $\nu = 2$.

due to its simple structure [24,26,50,52–55]. We review some features of the 2D CLM presented above in the context of experiments on ScF_3.

2D nanoscale correlations. Recent inelastic x-ray scattering work [18,56] has shown that ScF_3 features an incipient soft mode instability via its excitation spectrum. Specifically, the "central peak" phenomenon and a dispersionless branch of modes circumscribing the edges of the simple cubic Brillouin zone softens to zero temperature according to classical scaling and a putative transition temperature $T = -39$ K. The dispersionless nature of modes in one dimension of reciprocal space and observed diffuse x-ray scattering rods suggest a dimensional lowering in this system, permitting application of the 2D CLM [56]. We note the appearance of the system size in the expression for the lattice parameter [Eq. (6)], implying that the CTE vanishes in the thermodynamic limit. Comparison of the observed CTE and optic mode energy with literal application of the 2D CLM result presented in detail here implies a length scale ∼5–6 unit cells, in reasonable agreement with the correlation lengths observed in diffuse x-ray scattering data.

We note that the onset of CTE enhancement occurs at high temperatures, $k_B T > \hbar \omega_p / \nu$, where normal PTE may be activated by intramolecular distortions above the bond-bend threshold. This influence may contribute to the protracted temperature range where SNTE is observed [15,53].

Thermodynamics and finite-size effects. Anomalous thermodynamic behavior has been observed in SNTE materials ZrW_2O_8[48] and ScF_3 [49,50] which display unusually strong low-temperature heat capacity. Complications using Einstein-Debye fits of low-temperature heat capacity have been noted [49,57], suggesting there are interesting physics of SNTE materials manifest in their thermodynamical properties.

Recent studies of ScF_3 nanoparticles showing that both the CTE and low-temperature specific heat are enhanced in bulklike crystallites (∼1 μm) relative to nanoparticle samples (∼80 nm) with the same morphology, suggesting extensive scaling of thermal properties [50]. The peak in C_p/T^3 indicates an effective oscillator energy, which undergoes a sizable shift from 0.8 meV in bulk [49] samples to 4 meV for 80-nm nanoparticles [50]. In the language of the present model, variation of crystallite size is quantified by $N_x = \sqrt{N_\diamond} = k/\sqrt{\gamma}$. We have considered the size-dependent influences of the present model (e.g., $N_x \sim 200$ for 80-nm nanoparticles) and find through calculation that ν for these system sizes is only weakly dependent on N_x, too small of an effect to alone explain the magnitude of the observed trend in effective oscillator energy. Consistent with prior work, we attribute the size dependence to stiffening at small particle size [50]: In the language of our model, ω_p increases and ν decreases as the particles are reduced in size. Figures 4(c) and 5(b) show that a corresponding lowering of the CTE and stiffening of the C_p/T^3 peak are then expected to occur together in accord with experiments.

Long-period vibrations. Multiple MD simulations aimed at understanding the SNTE modes in the specific case of ScF_3 have been performed and dispersion data extracted [24,26,49,52–55]. In all but one tour-de-force study [53], these efforts produce mode energies at the M and R points of the simple cubic Brillouin zone in the range 5–10 meV, consistently higher than experiments

0.5–4 meV [18], suggesting that possibly the slow oscillations realized in the large k limit of our model are not captured in some finite-size simulations (low k in our model). The origin of the lengthened oscillation period in the 2D CLM is the large translational motion of molecules throughout the crystal and may be important to address in quantitative comparisons of computational results with experiments.

Angular distribution. We present the thermally-averaged probability distribution $P_T(\phi)$ for the angle $\phi = k\theta$ in Sec. 2 of the Appendix and in Fig. 4(a), showing that the low-temperature Gaussian distribution expected for the harmonic oscillator evolves into a two-peaked function at high temperatures. Recent MD simulations of ScF_3 at high temperature have revealed this surprising aspect of the probability distribution is highly non-Gaussian and that the system spends essentially zero time in the average structure with straight bonds [54,55]. This aspect is recovered in Sec. I of this paper [Fig. 2(b)], is explained using the pendulum analogy in Sec. 1 of the Appendix, and is resultant from the strong local constraints of the 2D CLM. We note that in contrast to our approach, MD simulations are at their heart semiclassical calculations and may be limited in capturing quantum mechanical aspects of the SNTE problem.

In conclusion, we have carried forth a thorough analysis of a model of SNTE that dates 20 years. We identified an important influence, the translational kinetic energy associated with the dilating lattice, and developed solutions for classical, quantum mechanical, and thermodynamical properties. We have presented exact analytical and numerical solutions, including expressions demonstrating strong enhancement of the CTE and thermodynamics. We contextualize the results and identify limited qualitative agreement with existing data. Further experimental work is required to characterize the quantum mechanical consequences of rigidity in SNTE materials.

APPENDIX

1. Archimedean spherical helix pendulum

Harmonic motion is intuitive, appears widely in physics, and sits at the heart of most approaches to lattice dynamics. The stark departure of features above can likewise be understood with basic mechanical intuition in a generalization of a planar pendulum, whose energy is given by (2) in the limit $k = 0$. The more general $k \neq 0$ case can be extended by recalling the kinetic energy of a particle moving in three dimensions expressed in spherical polar coordinates:

$$\frac{1}{2} m_P (\dot{r}^2 + r^2 \dot{\theta}^2 + r^2 \sin^2 \theta \dot{\phi}^2). \tag{A1}$$

TABLE I. The 2D CLM, characterized by parameters $N_\diamond I_\diamond$, I_c, and $N_b\kappa$, is dynamically equivalent to the Archimedean spherical pendulum with mass m_p, spherical radius R, and angular pitch λ in local gravity g according to the following mapping.

2D CLM	Archimedean spherical pendulum
$N_b\kappa$	$m_p g R$
$N_\diamond I_\diamond$	$m_p R^2$
$\omega_p^2 = N_b\kappa/N_\diamond I_\diamond$	g/R
$2\pi/k = 2\pi\sqrt{I_c/N_\diamond I_\diamond}$	λ

Constraining the particle position $\dot r = 0$, ($r = R$ constant) to a spherical surface, constraining the azimuthal and polar angles to each other $\phi = k\theta$, and identifying the parameter mapping spelled out in Table I establishes that the dynamics of the staggered rotation θ in the 2D CLM is equivalent to the dynamics of the polar angle of a particle constrained to move on an Archimedean spherical helix under local gravitation. Figure 6 shows two 2D CLMs of different size and their dynamically equivalent Archimedean spiral pendula (ASPs), plotted for illustration using the inertial parameters $m_\diamond a_0^2/I_\diamond = 10.74$ appropriate for ScF$_3$ and other oxide and fluoride perovskites. Importantly, the angular pitch of the helix is $\lambda = 2\pi/k = 2\pi\sqrt{\frac{N_\diamond I_\diamond}{I_c}}$, which tends to zero in the thermodynamic limit. In this context, we now develop an intuitive basis for the anharmonic features (i)–(iii) described in Sec. I.

(*i*) *Period is proportional to amplitude.* As gravity does work on a plane pendulum, it increases the linear speed
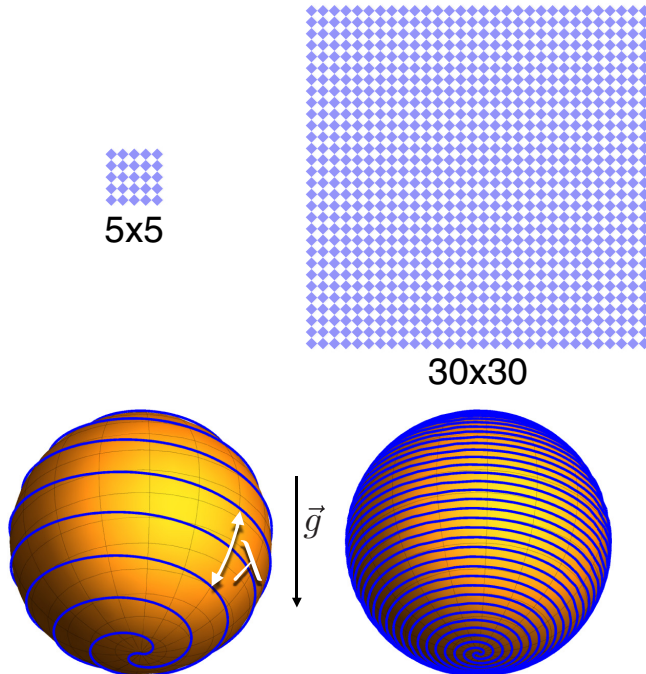

FIG. 6. (Top row) Example of small and large crystallites whose dynamics is governed by Eq. (2). (Bottom row) The corresponding Archimedean spherical helix pendulum with the same dynamics as the crystallite above it.

of the mass m_p during a quarter cycle along an arc length $s = R\theta_0$ and for small amplitudes, the period τ is independent of amplitude θ_0, as is well known: $\tau \propto (\theta_0)^0$. However, for the spiral case, the arc length threads many points on the conical cap of the sphere and the distance covered grows as the solid angle Ω subtended by a cone of apex half angle θ_0: $s = \Omega R^2/R\lambda = 2\pi R(1-\cos\theta)/\lambda \simeq R\theta_0^2 k/2$, and leads to an additional power of amplitude $\tau \propto (\theta_0)^1$ because of the higher-dimensional manifold of points visited within a cycle. Interestingly, this dimensional crossover in the zero-pitch limit of the ASP is also realized in the thermodynamic limit of the 2D CLM and may be a broadly important element of the dynamics of SNTE systems. The period is also proportional to the system size k and results from the vanishingly small component of gravitational force along the spiral path as $k \to \infty$.

(*ii*) *Vanishing probability density in average structure.* The linear speed of the mass m_p is largest in the polar region where the arc length within a narrow window $\Delta\theta$ is smallest and the resultant vanishing dwell time near the poles manifests as a node in the probability density $P(\theta)$ at $\theta = 0$. This peculiar property has been recovered in recent *ab initio* molecular dynamics simulations of ScF$_3$ at high temperature [54] in the computed probability density for the Sc-F-Sc bond. A three-dimensional extension of the present model is appropriate for direct comparison to these computational results.

(*iii*) *Moments of $P(\theta)$.* The larger variance of the classical probability distribution implies that the system spends longer time near the extrema of motion compared to the harmonic case. This feature is also intuitive in the ASP analog: The arc length in a small window of θ is larger near the equator than near the poles and the pendulum moves slowest near the turning points. This feature has direct implications for NTE: The time-averaged area $\langle A\rangle_t = A_0\langle\cos^2\theta(t)\rangle_t = A_0(1-\eta\theta_0^2)$. For the sinusoidal $k=0$ case, $\eta = 1/2$, while $\eta = 2/3$ for the thermodynamic limit $k\to\infty$, showing that the strain dynamics of CLMs enhances NTE over their harmonic counterparts. This strong enhancement of dimensional and orientational fluctuations is also realized when quantum and thermal effects are accounted for, as discussed further below.

The quantum mechanical treatment uses the variable $\phi = k\theta$, corresponding to the azimuthal angle of the ASP. We note that the solutions discussed here are also relevant to the quantum ASP and their analysis complements recent solutions of the quantum particle on a loxodrome [58]. The loxodrome (aka rhumb line) is another common spherical spiral which transforms to straight lines on a Mercator projection of a sphere and is best known for use in early naval navigation.

2. Expressions for contribution to thermal energy

In this section, we develop expressions for the thermally averaged angular variance and average energies of the 2D CLM. The partition function for the classical model, in the limit of small angle is

$$Z_{\rm cl} = \int_{-\infty}^{\infty} e^{-\beta H} d\theta dL_\theta$$
$$= e^\delta\sqrt{2\pi}\frac{k_B T}{\omega_p}[K_0(\delta) + K_1(\delta)],$$

where $\beta = 1/k_B T$, $\delta = \frac{N_b \kappa}{4k^2 k_B T}$, and $K_n(\delta)$ is the order n modified Bessel function of the second kind. The corresponding expression for the quantum model is

$$Z_{qu} = \sum_{n=0}^{\infty} e^{-\beta E_n}.$$

The thermally averaged second moment of θ is

$$\langle \theta^2 \rangle_{T,\text{cl}} = \frac{1}{Z_{\text{cl}}} \int \theta^2 e^{-\beta H} d\theta dL_\theta. \qquad \text{(A2)}$$

Evaluating this expression leads to Eq. (6). The corresponding expression for the quantum model is

$$\langle \theta^2 \rangle_{T,qu} = \frac{1}{Z_{qu}} \sum \langle n | \theta^2 | n \rangle e^{-\beta E_n}.$$

The thermally averaged probability distribution for the angle θ can be determined from

$$P_T(\theta) = \frac{1}{Z_{\text{cl}}} \int_{-\infty}^{\infty} e^{-\beta H} dL_\theta$$

$$= 2e^{-\delta(1+2k^2\theta^2)} \frac{k\sqrt{1+k^2\theta^2}}{[K_0(\delta) + K_1(\delta)]}$$

$$= k P_T(\phi).$$

The thermally averaged energy is

$$\langle E \rangle_{T,\text{cl}} = \frac{1}{Z_{\text{cl}}} \int_{-\infty}^{\infty} H e^{-\beta H} d\theta dL_\theta$$

$$= k_B T \left[1 + \frac{1}{2} \frac{K_1(\delta) - K_0(\delta)}{K_1(\delta) + K_0(\delta)} \right]$$

and

$$\langle E \rangle_{T,qu} = \frac{1}{Z_{qu}} \sum E_n e^{-\beta E_n}.$$

The thermally averaged rotational kinetic energy is

$$\langle K_{\text{rot}} \rangle_{T,\text{cl}} = \frac{1}{Z_{\text{cl}}} \int_{-\infty}^{\infty} \frac{L_\theta^2}{2N_\diamond I_\diamond (1+k^2\theta^2)^2} e^{-\beta H} d\theta dL_\theta$$

$$= k_B T \frac{K_0(\delta)}{K_1(\delta) + K_0(\delta)}.$$

The thermally averaged potential energy is

$$\langle V \rangle_{T,\text{cl}} = \frac{1}{Z_{\text{cl}}} \int_{-\infty}^{\infty} \frac{N_b \kappa}{2} \theta^2 e^{-\beta H} d\theta dL_\theta$$

$$= \frac{N_b \kappa}{2} \langle \theta^2 \rangle_{T,\text{cl}}$$

$$= k_B T \frac{K_1(\delta)}{K_1(\delta) + K_0(\delta)}.$$

TABLE II. Quantum parameters of the 2D CLM evaluated for representative perovskite-structured materials. Mean lattice parameters were evaluated in the cases where the symmetry is lowered by distortion and the A-site contribution, when present in the structure, was not addressed in the calculation. The trend shows that larger B-site masses have larger γ, and larger ν, and $\Delta\phi$. Calculations of ν and $\Delta\phi$ assume $\hbar\omega_p = 1$ meV.

Perovskite $\langle a \rangle$	(300 K)	γ	ν ($\omega_p = 1$ meV)	$\Delta\phi$ ($\hbar\omega_p = 1$ meV) (°)
ScF_3	4.014	1.79	0.0491	8.975
$SrTiO_3$	3.905	2.01	0.0689	10.62
$SrTcO_3$	3.95	3.07	0.1030	13.00
$SrRuO_3$	3.92	3.12	0.1061	13.20
ReO_3	3.742	4.90	0.1829	17.33
$SrIrO_3$	3.96	5.026	0.1676	16.58

The component not traditionally present in the harmonic oscillator is the thermally averaged potential energy:

$$\langle K_{\text{trans}} \rangle_{T,\text{cl}} = \frac{1}{Z_{\text{cl}}} \int_{-\infty}^{\infty} \frac{L_\theta^2 k^2 \theta^2}{2N_\diamond I_\diamond (1+k^2\theta^2)^2} e^{-\beta H} d\theta dL_\theta$$

$$= \frac{k_B T}{2} \left[\frac{K_1(\delta) - K_0(\delta)}{K_1(\delta) + K_0(\delta)} \right].$$

3. Assessment against other materials systems

Table II shows rough estimates of γ, ν, and $\Delta\phi$ for common interesting perovskite materials with formula ABX_3. The A-site contribution was ignored for simplicity (exact for open perovskites with formula BX_3), and $\hbar\omega_p = 1$ meV was assumed for the purposes of side-by-side comparison. The factor γ is calculated using the inertial parameters of the octahedra and assumes ideal cubic symmetry of the octahedra. This exercise reveals a trend suggesting heavier B-site elements tend to possess larger values of γ, ν, and $\Delta\phi$ and heavy perovskites exhibit larger deviation from harmonic behavior than their lighter counterparts. While experimental observation of quantized NTE modes awaits further experimental work and is beyond the scope of the present work, we suggest that a significant variation in ν could be accessed among known material systems and the results may be significant for a broad class of perovskite-structured materials. We speculate that near a structural phase transition where the effective soft optic mode describing octahedral rotation softens completely, the effective ω_p may become very small and, with a corresponding increase in ν, could exacerbate some of the features described here.

[1] C. E. Guillaume, Stockholm, Sweden: Royal Swedish Academy of Sciences pp. 1 (1920).

[2] J. Salvador, F. Guo, T. Hogan, and M. Kanatzidis, Nature (London) **425**, 702 (2003).

[3] Y. Janssen, S. Chang, B. Cho, A. Llobet, K. Dennis, R. McCallum, R. McQueeney, and P. Canfield, J. Alloys Compd. **389**, 10 (2005).

[4] M. Shiga, Curr. Opin. Solid State Mater. Sci. **1**, 340 (1996).

[5] S. Khmelevskyi, I. Turek, and P. Mohn, Phys. Rev. Lett. **91**, 037201 (2003).

[6] M. Azuma, W.-t. Chen, H. Seki, M. Czapski, S. Olga, K. Oka, M. Mizumaki, T. Watanuki, N. Ishimatsu, N. Kawamura *et al.*, Nat. Commun. **2**, 347 (2011).

[7] K. Oka, M. Mizumaki, C. Sakaguchi, A. Sinclair, C. Ritter, J. P. Attfield, and M. Azuma, Phys. Rev. B **88**, 014112 (2013).

[8] K. Takenaka, Y. Okamoto, T. Shinoda, N. Katayama, Y. Sakai, C. N. Chu, N. Saka, N. P. Suh, A. W. Sleight, G. D. Barrera *et al.*, Nat. Commun. **8**, 14102 (2017).

[9] F. Ji, X. Dai, R. Stevens, and J. B. Goates, Sci. China Phys., Mech. Astron. **55**, 563 (2012).

[10] R. Mittal, S. L. Chaplot, H. Schober, A. I. Kolesnikov, C.-K. Loong, C. Lind, and A. P. Wilkinson, Phys. Rev. B **70**, 214303 (2004).

[11] A. L. Goodwin, M. Calleja, M. J. Conterio, M. T. Dove, J. S. O. Evans, D. A. Keen, L. Peters, and M. G. Tucker, Science (New York, NY) **319**, 794 (2008).

[12] A. W. Sleight, Curr. Opin. Solid State Mater. Sci. **3**, 128 (1998).

[13] R. Mittal, S. L. Chaplot, H. Schober, and T. A. Mary, Phys. Rev. Lett. **86**, 4692 (2001).

[14] J. C. Hancock, K. W. Chapman, G. J. Halder, C. R. Morelock, B. S. Kaplan, L. C. Gallington, A. Bongiorno, C. Han, S. Zhou, and A. P. Wilkinson, Chem. Mater. **27**, 3912 (2015).

[15] B. K. Greve, K. L. Martin, P. L. Lee, P. J. Chupas, K. W. Chapman, and A. P. Wilkinson, J. Am. Chem. Soc. **132**, 15496 (2010).

[16] E. E. Rodriguez, A. Llobet, T. Proffen, B. C. Melot, R. Seshadri, P. B. Littlewood, and A. K. Cheetham, J. Appl. Phys. **105**, 114901 (2009).

[17] C. R. Morelock, L. C. Gallington, and A. P. Wilkinson, Chem. Mater. **26**, 1936 (2014).

[18] S. U. Handunkanda, E. B. Curry, V. Voronov, A. H. Said, G. G. Guzman-Verri, R. T. Brierley, P. B. Littlewood, and J. N. Hancock, Phys. Rev. B **92**, 134101 (2015).

[19] M. T. Dove and H. Fang, Rep. Prog. Phys. **79**, 066503 (2016).

[20] M. G. Tucker, A. L. Goodwin, M. T. Dove, D. A. Keen, S. A. Wells, and J. S. O. Evans, Phys. Rev. Lett. **95**, 255501 (2005).

[21] A. L. Goodwin and C. J. Kepert, Phys. Rev. B **71**, 140301(R) (2005).

[22] D. Cao, F. Bridges, G. R. Kowach, and A. P. Ramirez, Phys. Rev. Lett. **89**, 215902 (2002).

[23] F. Bridges, T. Keiber, P. Juhas, S. J. L. Billinge, L. Sutton, J. Wilde, and G. R. Kowach, Phys. Rev. Lett. **112**, 045505 (2014).

[24] S. Piskunov, P. A. Žguns, D. Bocharov, A. Kuzmin, J. Purans, A. Kalinko, R. A. Evarestov, S. E. Ali, and F. Rocca, Phys. Rev. B **93**, 214101 (2016).

[25] A. Sanson, Chem. Mater. **26**, 3716 (2014).

[26] J. T. Schick and A. M. Rappe, Phys. Rev. B **93**, 214304 (2016).

[27] J. Tao and A. Sleight, J. Solid State Chem. **173**, 442 (2003).

[28] J. N. Grima, P. S. Farrugia, R. Gatt, and V. Zammit, Proc. R. Soc. London, Ser. A **463**, 1585 (2007).

[29] W. Miller, C. W. Smith, D. S. Mackenzie, and K. E. Evans, J. Mater. Sci. **44**, 5441 (2009).

[30] C. Lind, Materials **5**, 1125 (2012).

[31] K. Takenaka, Sci. Technol. Adv. Mater. **13**, 013001 (2012).

[32] A. Souslov, A. J. Liu, and T. C. Lubensky, Phys. Rev. Lett. **103**, 205503 (2009).

[33] X. Mao, N. Xu, and T. C. Lubensky, Phys. Rev. Lett. **104**, 085504 (2010).

[34] K. Sun, A. Souslov, X. Mao, and T. C. Lubensky, Proc. Natl. Acad. Sci. USA **109**, 12369 (2012).

[35] C. L. Kane and T. C. Lubensky, Nat. Phys. **10**, 39 (2013).

[36] J. Clerk Maxwell, Phil. Mag. Ser. 4 **27**, 294 (1864).

[37] C. R. Calladine, Int. J. Solids Stru. **14**, 161 (1978).

[38] P. R. L. Welche, V. Heine, and M. T. Dove, Phys. Chem. Miner. **26**, 63 (1998).

[39] P. Sollich, V. Heine, and M. T. Dove, J. Phys.: Condens. Matter **6**, 3171 (1994).

[40] M. E. Simon and C. M. Varma, Phys. Rev. Lett. **86**, 1781 (2001).

[41] Z. Schlesinger, J. A. Rosen, J. N. Hancock, and A. P. Ramirez, Phys. Rev. Lett. **101**, 015501 (2008).

[42] Y. He, V. Cvetkovic, and C. M. Varma, Phys. Rev. B **82**, 014111 (2010).

[43] Throughout the paper, when we calculate the moments of inertia of crystals and diamonds, we consider the arrangement of atoms in a perovskite octahedron and split the mass of atoms at the corners. For example, an octahedral system ABX_3 with simple cubic lattice parameter a_0 will have a moment of inertia $I_\diamond = 4 \times (m_X/2)(a_0/2)^2$ and mass $m_\diamond = m_B + 6 \times (m_X/2)$. We have ignored the A-site contribution for simplicity. For ScF_3, $m_{oct} = 102$ amu, $I_\diamond = I_{oct}$, and $\gamma = 1.79$.

[44] Equation (5) can be obtained by taking the small-angle limit, setting the energy $E = 1/2N_b\kappa\theta_0^2$, using $P(\theta) \propto 1/\dot\theta$, and normalizing.

[45] J. N. Hancock, G. Chabot-Couture, and M. Greven, New J. Phys. **12**, 033001 (2010).

[46] R. G. Chambers, Proc. Phys. Soc. **78**, 941 (1961).

[47] A. Junod, T. Jarlborg, and J. Muller, Phys. Rev. B **27**, 1568 (1983).

[48] A. P. Ramirez and G. R. Kowach, Phys. Rev. Lett. **80**, 4903 (1998).

[49] C. P. Romao, C. R. Morelock, M. B. Johnson, J. W. Zwanziger, A. P. Wilkinson, and M. A. White, J. Mater. Sci. **50**, 3409 (2015).

[50] C. Yang, P. Tong, J. C. Lin, X. G. Guo, K. Zhang, M. Wang, Y. Wu, S. Lin, P. C. Huang, W. Xu *et al.*, Appl. Phys. Lett. **109**, 023110 (2016).

[51] J. N. Hancock, C. Turpen, Z. Schlesinger, G. R. Kowach, and A. P. Ramirez, Phys. Rev. Lett. **93**, 225501 (2004).

[52] C. W. Li, X. Tang, J. A. Muñoz, J. B. Keith, S. J. Tracy, D. L. Abernathy, and B. Fultz, Phys. Rev. Lett. **107**, 195504 (2011).

[53] A. van Roekeghem, J. Carrete, and N. Mingo, Phys. Rev. B **94**, 020303 (2016).

[54] P. Lazar, T. Bucko, and J. Hafner, Phys. Rev. B **92**, 224302 (2015).

[55] D. Bocharov, M. Krack, A. Kalinko, J. Purans, F. Rocca, S. E. Ali, and A. Kuzmin, J. Phys.: Conf. Ser. **712**, 012009 (2016).

[56] S. U. Handunkanda, C. A. Occhialini, A. H. Said, and J. N. Hancock, Phys. Rev. B **94**, 214102 (2016).

[57] X.-G. Guo, J.-C. Lin, P. Tong, S. Lin, C. Yang, W.-J. Lu, W.-H. Song, and Y.-P. Sun, Chin. Phys. B **26**, 026501 (2017).

[58] D. S. Tourigny, Mod. Phys. Lett. B **26**, 1250052 (2012).